mater.scichina.com link.springer.com

Published online 31 August 2021 | https://doi.org/10.1007/s40843-021-1754-7
*Sci China Mater* 2022, 65(1): 43–50

# Anchoring ultrafine CoP and CoSb nanoparticles into rich N-doped carbon nanofibers for efficient potassium storage

Jingyi Xu[†], Chenling Lai[†], LiPing Duan, Yuxuan Zhang, Yifan Xu, Jianchun Bao and Xiaosi Zhou[*]

**ABSTRACT Transition-metal compounds have received extensive attention from researchers due to their high reversible capacity and suitable voltage platform as potassium-ion battery anodes. However, these materials commonly feature a poor conductivity and a large volume expansion, thus leading to underdeveloped rate capability and cyclic stability. Herein, we successfully encapsulated ultrafine CoP and CoSb nanoparticles into rich N-doped carbon nanofibers (NCFs) *via* electrospinning, carbonization, and phosphorization (antimonidization). The N-doped carbon fiber prevents the aggregation of nanoparticles, buffers the volume expansion of CoP and CoSb during charging and discharging, and improves the conductivity of the composite material. As a result, the CoP/NCF anode exhibits excellent potassium-ion storage performance, including an outstanding reversible capacity of 335 mA h $g^{-1}$, a decent capacity retention of 79.3% after 1000 cycles at 1 A $g^{-1}$ and a superior rate capability of 148 mA h $g^{-1}$ at 5 A $g^{-1}$, superior to most of the reported transition-metal-based potassium-ion battery anode materials.**

**Keywords:** CoP, CoSb, N-doped carbon nanofibers, anode, potassium-ion batteries

## INTRODUCTION

Owing to the high specific capacity and power density, lithium-ion batteries (LIBs) have become one of the most important and ubiquitous energy storage systems that are widely used in portable electronic devices [1,2]. However, lithium in the earth crust is inadequate and unevenly distributed, making it difficult to apply to large-scale energy storage systems such as electric vehicles and smart grids [3–6]. The reserve of potassium in the earth crust is more than a thousand times that of lithium, and the volume of solvated potassium ions is relatively small [7]. Therefore, potassium-ion batteries (PIBs) are considered to be a promising large-scale energy storage system [8,9]. In recent years, researchers have carried out a series of studies on potential PIB anode materials such as carbon materials [10], transition metal compounds [11], organic compounds [12], and alloy materials [13]. However, it is still an arduous challenge to synthesize an anode material with high energy density and cyclic stability.

Transition metal compounds usually have high reversible capacities, suitable discharge voltages, and easily available raw materials [14,15]. Nevertheless, when potassium ions are intercalated/deintercalated, transition metal compounds often generate a large volume expansion (>80% for CoP), which could cause the collapse and powdering of the material structures. There are three common strategies to diminish the impact of volume expansion: designing hollow structures [16], reducing particle size [17], and coating carbon materials [18,19]. But it is worth mentioning that although the hollow structure could provide extra buffering space for volume expansion, it would substantially reduce the volume energy density [20]. The hollow architecture of active materials would also be inevitably damaged when they are ground with the binder and carbon black. Therefore, the preparation of carbon-incorporated transition metal compounds with tiny nanoparticle size is the key to the practical application of PIBs [21–23].

Herein, we report a universal synthesis method, which takes well-dispersed ZIF-67 in polyacrylonitrile (PAN)/*N*,*N*-dimethylformamide (DMF) solution as the precursor, and uniformly encapsulates ultrafine carbon-coated CoP and CoSb nanoparticles into rich N-doped carbon nanofibers (NCFs) through electrospinning, carbonization, and subsequent phosphorization (antimonidization). The confining effect between CFs and Co particles can prevent nanoparticles from aggregation during the pyrolysis process. The carbon coating layer *in-situ* forms and the rich NCFs can provide a double buffer for the volume expansion, improving the stability and conductivity of the composite material. When used as an anode material for PIB, the reversible capacities of CoP/NCF and CoSb/NCF are as high as 335 and 311 mA h $g^{-1}$, respectively. Even under a high current density of 5 A $g^{-1}$, CoP/NCF and CoSb/NCF can still maintain decent capacities of 148 and 96 mA h $g^{-1}$, respectively. In addition, CoP/NCF and CoSb/NCF also exhibit superior cyclic stability at 1 A $g^{-1}$, confirming their great potential for practical applications.

## EXPERIMENTAL SECTION

### Preparation of ZIF-67/DMF suspension

In the first step, 1.456 g of $Co(NO_3)_2{\cdot}6H_2O$ (99%, Aladdin) was dissolved in 50 mL of DMF to form a uniform purple-red solution (liquid A). Then, 3.28 g of 2-methylimidazole (99%, Aladdin) was dissolved in 50 mL of DMF to form another uniform and transparent solution (liquid B). Afterwards, the liquid B was quickly poured into the liquid A and vigorously stirred for

Jiangsu Key Laboratory of New Power Batteries, Jiangsu Collaborative Innovation Center of Biomedical Functional Materials, School of Chemistry and Materials Science, Nanjing Normal University, Nanjing 210023, China
[†] These authors contributed equally to this work.
[*] Corresponding author (email: zhouxiaosi@njnu.edu.cn)

  

2 h. The as-formed suspension was centrifuged and washed with ethanol and DMF for several times. A part of the wet sample (the content of ZIF-67 was approximately 0.5 g) was taken and dispersed evenly in 10 mL of DMF to prepare a ZIF-67/DMF suspension. The remaining sample was dried at 70°C overnight in an oven to obtain ZIF-67 purple powder.

**Preparation of Co/NCF**

For the synthesis of Co/NCF, 0.7 g of PAN was added to the ZIF-67/DMF suspension and stirred at 60°C for 12 h to produce a homogeneous purple dispersion. Then the dispersion was injected into a 10-mL syringe and electrospun at a voltage of 15 kV. The flow rate was controlled to be 0.3 mL $h^{-1}$, and the distance between the needle and the aluminum foil was kept at 12 cm. Finally, the electrospun film was carbonized at 625°C for 30 min under a $H_2$/Ar (5:95 in volume ratio) environment with a heating rate of 1°C $min^{-1}$ to obtain Co/NCF.

**Preparation of CoP/NCF**

With a mass ratio of 1:10, Co/NCF and $NaH_2PO_2$ (99%, Aladdin) were placed on the two ends of a porcelain boat ($NaH_2PO_2$ at the upper wind), and heated at 600°C for 3 h in a $H_2$/Ar (5:95 in volume ratio) atmosphere to get CoP/NCF. The ramping rate was set to be 5°C $min^{-1}$.

**Preparation of CoSb/NCF**

Co/NCF and Sb powders (99%, Aladdin) in a mass ratio of 1:1 were placed on both ends of a porcelain boat (Sb powder was placed on the upper wind). Subsequently, the sample was heated in a $H_2$/Ar (5:95 in volume ratio) atmosphere at 650°C for 2 h with the heating rate of 5°C $min^{-1}$ to obtain CoSb/NCF.

**Material characterization**

The crystal structure of the samples was characterized on an X-ray diffractometer (XRD, Rigaku SmartLab) with a Cu target. The morphology of the samples was characterized using field emission scanning electron microscopy (FESEM, JEOL JSM-7600F) and transmission electron microscopy (TEM, Talos F200X). To unveil the element composition of the product, X-ray photoelectron spectroscopy (XPS) spectrum was collected on an X-ray spectrometer (ESCALab250Xi) equipped with an Al target. The Raman fingerprints were recorded on a Labram HR800. Nitrogen sorption isotherms were measured on an ASAP 2050 surface analyzer. The NETZSCH STA 449 F3 thermogravimetric analyzer (TGA) was used to gauge the thermogravimetric curve of the as-synthesized materials.

**Electrochemical characterization**

For the preparation of the working electrode, active materials, Super-P carbon black, and polyvinylidene fluoride (PVDF) binder were grinded at a mass ratio of 8:1:1, and evenly spread on a Cu foil. Then the electrode was dried overnight in a vacuum drying oven at 80°C. The mass of the active material was controlled to be 0.8–1.2 mg $cm^{-1}$. The battery assembly process was carried out in a glove box (MBRAUN) filled with Ar gas. The water and oxygen contents were controlled below 0.1 ppm during the whole process. Potassium sheet was used as the counter electrode. Whatman glass fiber was adopted as the separator, and the electrolyte was 1.5 mol $L^{-1}$ potassium bis (fluorosulfonyl)imide (KFSI) in a solution of ethylene carbonate (EC) and diethyl carbonate (DEC) (1:1 in volume). The galvanostatic charging and discharging performance was tested on a Land CT2001A battery test system. Cyclic voltammetry (CV) curves were measured by a PARSTAT 4000 electrochemical workstation.

## RESULTS AND DISCUSSION

Fig. 1 illustrates the synthetic route of CoP/NCF and CoSb/NCF. During the synthesis, ZIF-67 was adopted as the precursor of Co. Its structural information and exterior morphology are displayed in Figs S1, S2. It can be detected that the average diameter of the dried ZIF-67 nanoparticles (~50 nm, Fig. S2a) is larger than that of the ZIF-67 nanoparticles dispersed in DMF (~20 nm, Fig. S2b). This is the reason why the ZIF-67/DMF suspension was selected for electrospinning rather than using dried ZIF-67 particles. Fig. S3 demonstrates the XRD pattern of Co/NCF, implying the amorphous nature of the CF and well crystallinity of Co. Applying the Scherrer equation to the (111) characteristic peak of Co, the average Co size is calculated to be around 10 nm. The SEM and TEM images (Fig. S4) further unravel the uniform

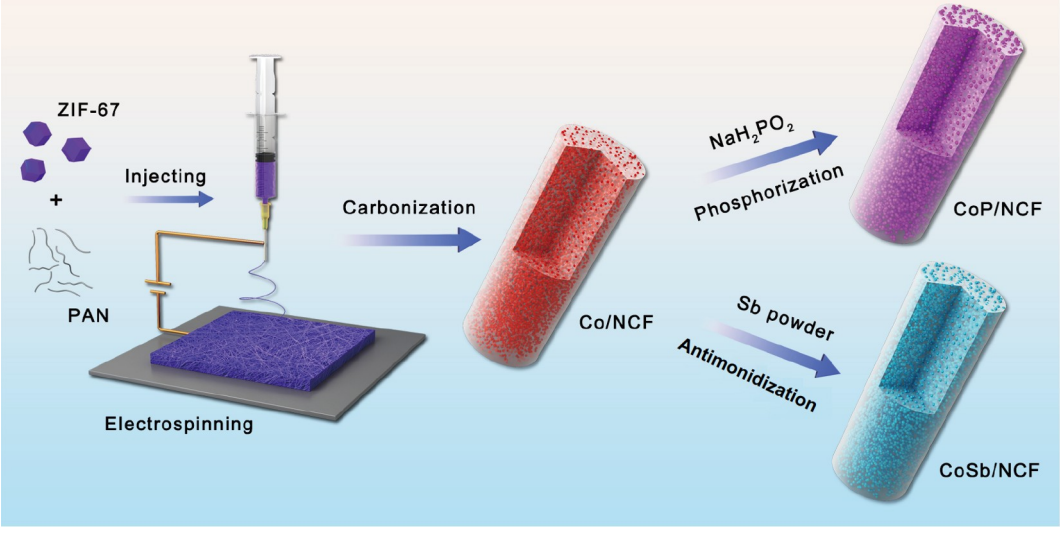


**Figure 1** Schematic illustration for the preparation of CoP/NCF and CoSb/NCF.

nanofiber morphology, high Co content and the ultrafine particle size. TGA results (Fig. S5) demonstrate that the Co content in Co/NCF is about 29.2 wt%. Further, CoP and CoSb content in CoP/NCF and CoSb/NCF can be accordingly calculated to be 38.6 and 55.8 wt%, respectively. To further decrease the carbon contents in CoP/NCF and CoSb/NCF, we increased the concentration of ZIF-67 in the electrospinning precursor dispersion; however, augmenting the ZIF-67 amount resulted in the aggregation of Co particles (Fig. S6), which was harmful to the formation of ultrasmall CoP and CoSb nanoparticles.

Using $NaH_2PO_2$ as the phosphorization reagent, Co/NCF was phosphorated at 600°C to produce CoP/NCF, whose morphology is demonstrated in Fig. 2. The XRD pattern shown in Fig. 2a verifies the successful fabrication of CoP [24]. Fig. 2b, c display the one-dimensional architecture of CoP/NCF, which features a uniform fiber diameter of around 280 nm and a rough exterior surface. The TEM image in Fig. 2d demonstrates the ultrasmall particle size (~13 nm) of the well-dispersed CoP. The nanosized particles are favorable for shortening the $K^+$ diffusion distance and mitigating the impact of volume expansion, thereby contributing to the rate capability and cyclic stability of potassium-ion batteries [25]. Fig. 2e presents the high-resolution TEM (HRTEM) image, where the amorphous carbon layer can be detected. Nonetheless, the lattice of CoP is too faint to be clearly observed. This is because of the low crystallinity of CoP, in good agreement with the XRD result. Fig. 2f–j exhibit the energy dispersive X-ray (EDX) elemental mapping results of C, N, Co, and P in CoP/NCF, showing the even distribution of CoP in NCF. Fig. S7 demonstrates the overlapped mapping image and linear scanning results, which also imply the homogeneous distribution of the existing elements and the high content of N.

To obtain CoSb/NCF, Co/NCF was annealed with antimony powder at 650°C for 2 h. Fig. 3a shows the XRD pattern of CoSb/NCF. The sharp peaks at about 31.6°, 44.2°, and 46.9° correspond to the (101), (102), and (110) lattice planes, respectively, suggesting the successful synthesis of CoSb. SEM and TEM images uncover the detailed morphology of CoSb/NCF. As can be seen in Fig. 3b, c, the diameter of CoSb/NCF is around 250 nm, substantially smaller than that of CoP/NCF. Fig. 3d manifests a particle size (~15 nm) of CoSb. In spite of the relatively low crystallinity, lattice fringe that represents the (101) plane can be observed in the HRTEM image (Fig. 3e). The inferior crystallinities of CoP/NCF and CoSb/NCF could be ascribed to the ultrasmall particle sizes and the relatively low active material contents. EDX mapping was also carried out to qualitatively reveal the element composition and distribution in CoSb/NCF. As shown in Fig. 3f–j, CoSb particles do not disperse as evenly as CoP, while they still fill the major room of the CFs. Furthermore, the overlapped mapping image and linear scanning results further unveil the existence of C, N, Co, and Sb elements and the rich N content (Fig. S8).

To quantitatively examine the element compositions of CoP/

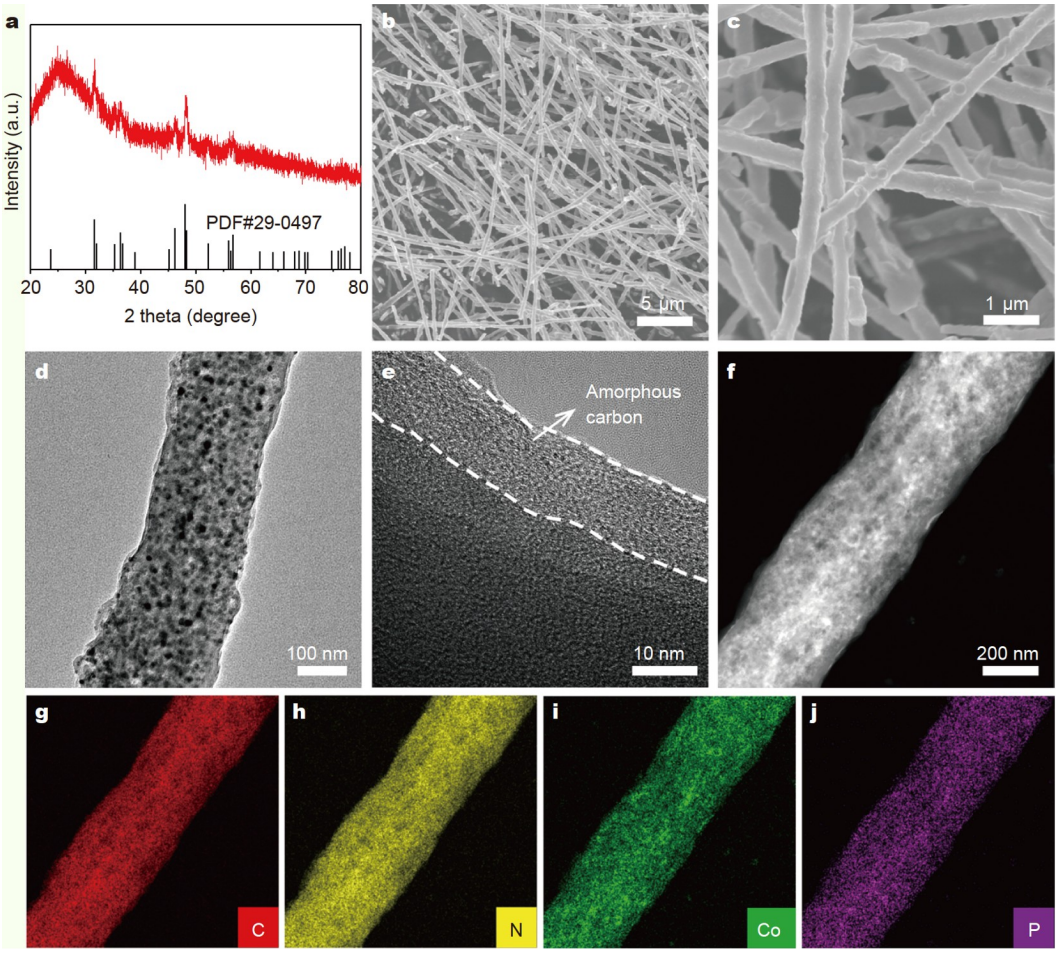


**Figure 2** (a) XRD pattern, (b, c) SEM images, (d) TEM image, (e) HRTEM image, and (f–j) elemental mappings of CoP/NCF.

  

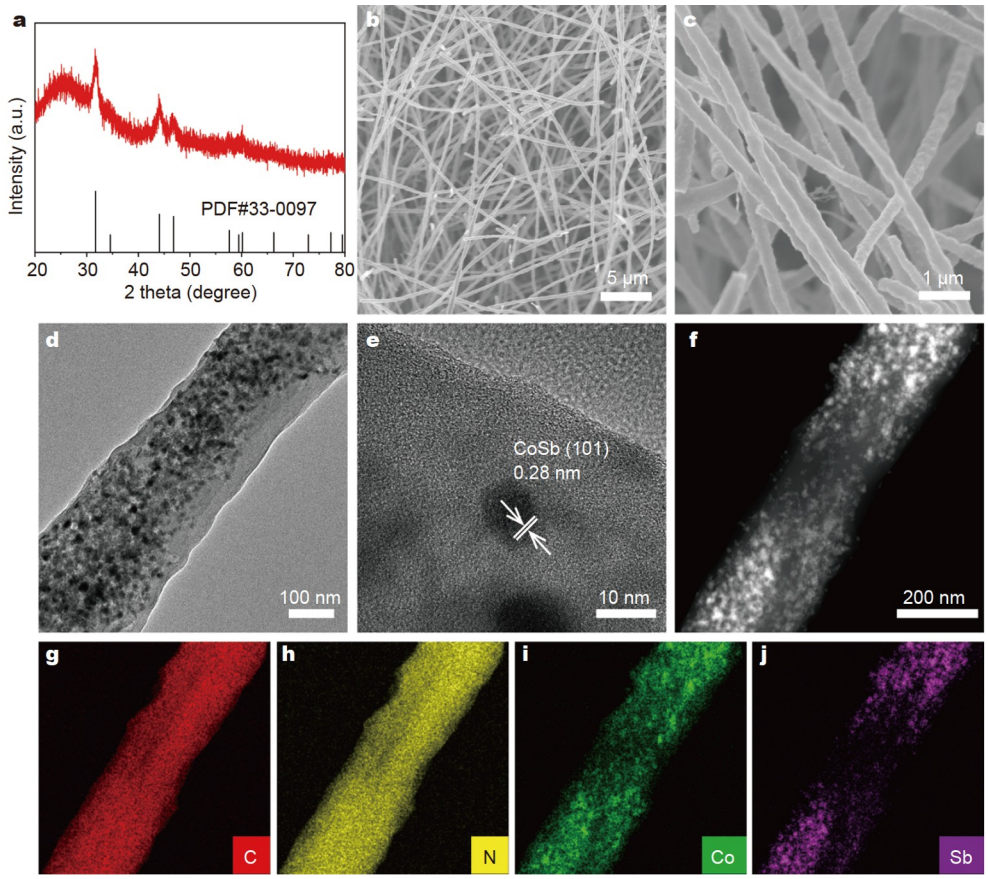


**Figure 3** (a) XRD pattern, (b, c) SEM images, (d) TEM image, (e) HRTEM image, and (f–j) elemental mappings of CoSb/NCF.

NCF and CoSb/NCF, XPS spectra were further studied. Figs S9, S10 display the XPS full spectra of CoP/NCF and CoSb/NCF, whose N atomic percentages are measured to be 18.5% and 15.7%, respectively. The rich N dopant could elevate the concentration of electrons and increase the conductivity of the materials [26]. The high-resolution Co 2p spectra (Fig. 4a, d) show that the Co $2p_{3/2}$ peak is at 781.4 eV with its accompanying peak located at 786.3 eV, while the Co $2p_{1/2}$ peak locates at 797.1 eV, and its satellite peak is at 803.0 eV, which are close to the literature values [27,28]. The positions and peak shapes of the Co 2p peaks of CoP/NCF and CoSb/NCF are identical, which proves that the Co elements in these two composites have similar +3 valent state and electronic structures. In addition, the C 1s spectra of CoP/NCF and CoSb/NCF (Fig. 4b, e) both reveal the existence of C-C/C=C, C-O, and C-N bonds, indicating that the CFs possess plenty of defects and heteroatom dopants. Interestingly, in the N 1s spectra (Fig. 4c, f), it can be probed that the graphitic N occupies a large proportion of the N in CoP/NCF, while the N in CoSb/NCF merely consists of pyridinic and pyrrolic N. The state transference of N could be ascribed to the fact that the antimonidization process causes a larger damage to the carbon matrix, thus exposing more N atoms at the margin of the amorphous carbon. Brunauer–Emmett–Teller measurement was also conducted to study the porosity of samples. Fig. 4g, h demonstrate that CoP/NCF and CoSb/NCF possess a large surface area of 259 and 190 $m^2 g^{-1}$, and are featured with bountiful micropores and mesopores. The micropores are inherited from the CFs, while the mesopores are attributed to the disintegration of ZIF-67 and PAN. The considerable surface area and hierarchical pore size distribution are beneficial to electrolyte infiltration and high-rate performance [29]. Fig. 4i exhibits the Raman spectra, from which the $I_D/I_G$ ratios of CoP/NCF and CoSb/NCF are computed to be 1.33 and 1.43, respectively, indicating a larger disorder degree in the carbon framework of CoSb/NCF. The small peak at 700 $cm^{-1}$ is assigned to the $A_{1g}$ vibration mode of $Co_3O_4$, indicating the partial surface oxidation of the CoSb/NCF sample.

After the materials were assembled as the anodes of PIBs, the potassium storage performances of CoP/NCF and CoSb/NCF were evaluated. Fig. 5a shows the CV curves of CoP/NCF at a sweep rate of 0.1 mV $s^{-1}$. During the first positive scan of CoP/NCF, two obvious reduction peaks appear at 0.18 and 0.58 V. This is due to the initial insertion of potassium ions and the decomposition of the electrolyte on the electrode surface to form a solid electrolyte interface (SEI) phase [30]. In the next two scans, the positive sweep peak at around 0.29 V and the negative sweep peak at ~2.0 V emerge, representing the reversible insertion/extraction reaction of potassium ions. The charging and discharging curves of the first three cycles (Fig. 5b) are consistent with the CV curves. Among them, the profiles of the last two cycles are overlapped, indicating that the intercalation/disintercalation behavior of potassium ions in CoP/NCF is highly reversible. The reversible specific capacity of CoP/NCF is measured to be 335 mA h $g^{-1}$. Fig. 5c shows the CV curves of CoSb/NCF at a sweep speed of 0.1 mV $s^{-1}$. The reduction peaks at 0.01 and 0.58 V are related to the intercalation behavior of potassium ions in carbon and CoSb and the formation of SEI film [31]. Correspondingly, potassium ions are gradually

  

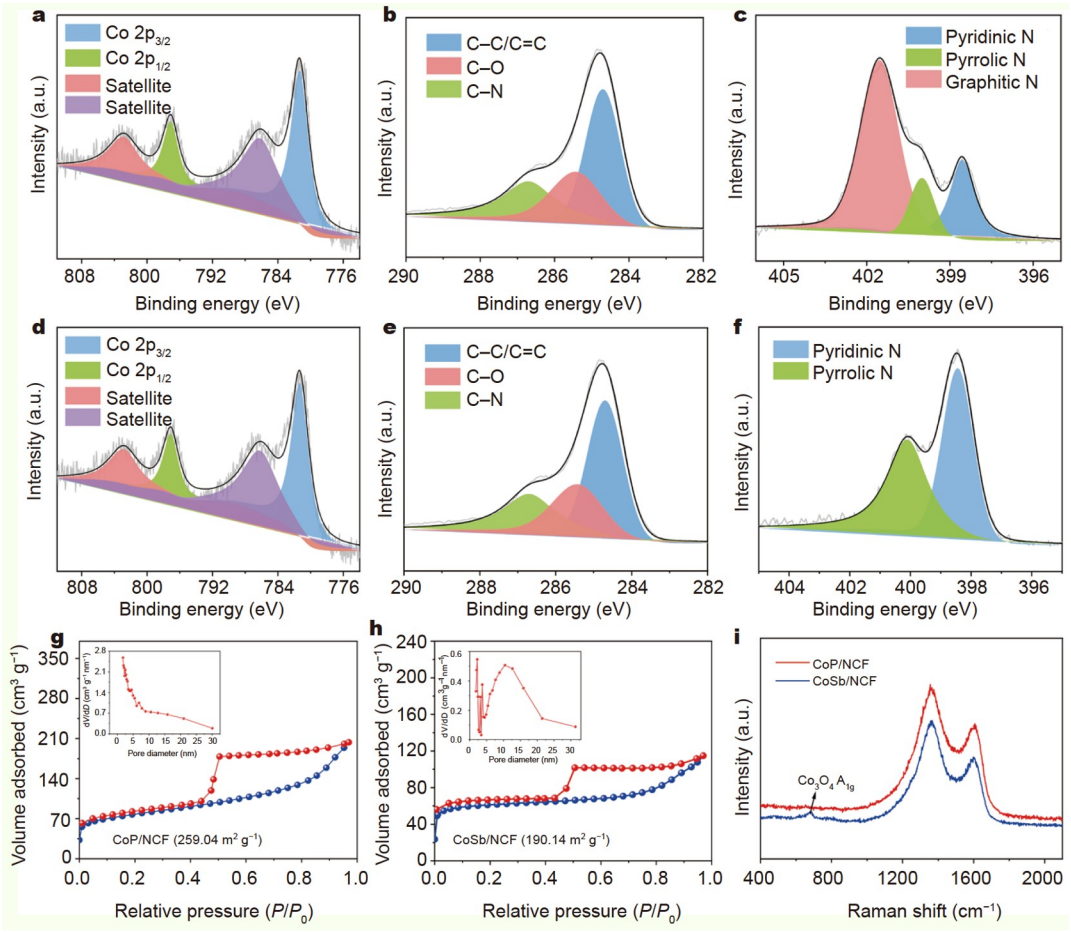


**Figure 4** High-resolution (a, d) Co 2p, (b, e) C 1s, and (c, f) N 1s XPS spectra of CoP/NCF and CoSb/NCF. Nitrogen sorption isotherms and pore-size distributions of (g) CoP/NCF and (h) CoSb/NCF. (i) Raman spectra of CoP/NCF and CoSb/NCF.

released at approximately 0.52 and 1.09 V, like the previously reported literature data. The galvanostatic charging and discharging curves (Fig. 5d) demonstrate that the reversible capacity of CoSb/NCF at 0.1 A $g^{-1}$ is about 311 mA h $g^{-1}$.

Fig. 5e manifests the rate capability of the samples. At current densities of 0.1, 0.2, 0.5, 1, 2, and 5 A $g^{-1}$, the reversible capacities of CoSb/NCF are 295, 242, 209, 170, 141 and 96 mA h $g^{-1}$, respectively, showing good rate performance. Under the same current densities of 0.1–2 A $g^{-1}$, CoP/NCF exhibits higher reversible capacities of 327, 284, 249, 214, and 180 mA h $g^{-1}$. Even at a high current rate of 5 A $g^{-1}$, CoP/NCF can maintain a superior capacity of 148 mA h $g^{-1}$, exceeding that of the CoSb/NCF nanocomposite. The corresponding charging/discharging profiles at diverse rates are illustrated in Fig. S11. The better rate performance of CoP/NCF is derived from the higher theoretical capacity, more uniform active nanoparticle distribution, and richer N content.

CoP/NCF and CoSb/NCF also display extraordinary cyclic stability. Specifically, when cycled at 0.1 A $g^{-1}$, CoP/NCF and CoSb/NCF can maintain superior capacities of 301 and 276 mA h $g^{-1}$ after 200 cycles (Fig. 5f). When a larger current of 1 A $g^{-1}$ is exerted, CoP/NCF and CoSb/NCF still display decent capacity retentions of 79.3% and 79.9% after 1000 cycles, respectively (Fig. S12). Note that the batteries were directly tested at 1 A $g^{-1}$ without activation at low current densities, so the initial capacities are inferior to the results presented in Fig. 5e.

These excellent electrochemical properties exceed most of the previously reported transition-metal compounds (Table S1) [32,33]. To examine the structural stability of CoP/NCF and CoSb/NCF, the morphologies of the cycled samples are manifested in Figs S13, S14. Even after 1000 cycles at a high current density of 1 A $g^{-1}$, the one-dimensional architectures of CoP/NCF and CoSb/NCF remain intact, proving the outstanding structural integrity. It is worth noting that the extraordinary performance is mainly attributed to the double-layer carbon coating that buffers the volume expansion of the material and improves the electrical conductivity [34]. Additionally, the ultrasmall particle size is conducive to increasing the contact area between the electrolyte and the electrode, exposing more active reaction sites, and increasing the actual capacity of the battery.

To figure out the potassium storage mechanisms of CoP/NCF and CoSb/NCF, CV curves were recorded at different scanning rates from 0.1 to 10 mV $s^{-1}$ in Figs S15, S16. The ion transport and reaction kinetics were evaluated according to the equation: $i = av^b$, where $i$ represents the responding peak current, $v$ refers to the scan rate; $a$ and $b$ are the constants [35]. As shown in Fig. S16b, the $b$ values of the cathodic and anodic peaks for CoP/NCF range from 0.66 to 0.96, reflecting a combined ion storage mechanism. The capacitive and diffusion-governed capacities were further calculated *via* the equation $i(V) = k_1v + k_2v^{1/2}$,

  

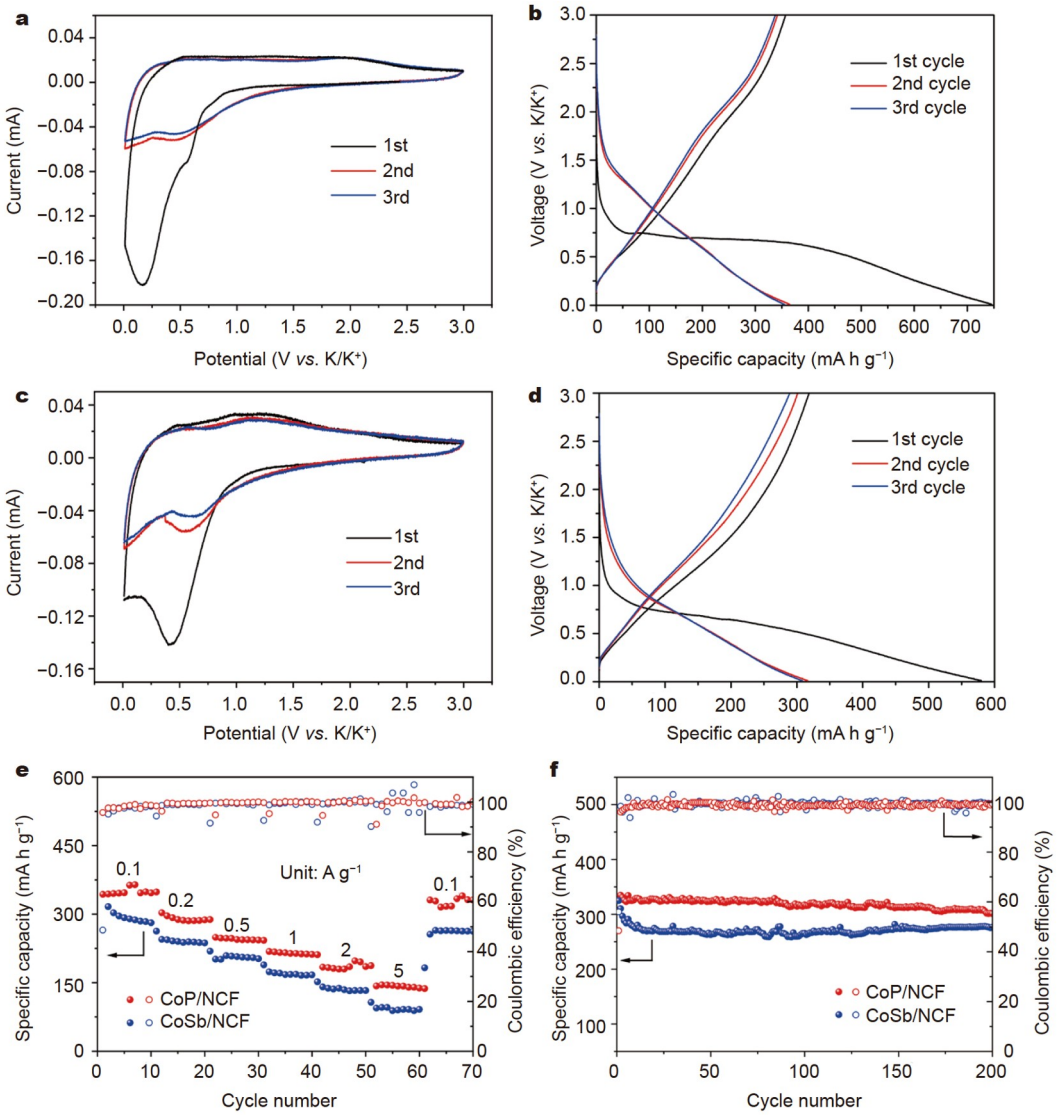


**Figure 5** (a, c) CV curves and (b, d) charging/discharging profiles for CoP/NCF and CoSb/NCF. (e) Rate capabilities and (f) cycling performances of CoP/NCF and CoSb/NCF.

where $k_1v$ stands for the capacitive-controlled portion [36]. As the scan rate increases, the capacitive contribution gradually enlarges from 18.8% (0.4 mV $s^{-1}$) to 61.9% (10 mV $s^{-1}$), suggesting a diffusion-dominated process at slow scan rates. Compared with CoP/NCF, the capacitive contributions of CoSb/NCF at diverse scan rates are relatively larger (Fig. S16).

## CONCLUSIONS

In summary, we report a universal multi-step synthesis strategy that incorporates ultrafine CoP (CoSb) nanoparticles with a diameter of less than 15 nm into rich NCFs to achieve CoP/NCF and CoSb/NCF nanocomposites with high active-substance contents. Due to the synergistic effect of nanoparticles and the conductive carbon supporting nanofibers, CoP/NCF and CoSb/NCF exhibit excellent potassium storage properties, including high reversible capacities, excellent rate performance, and cyclic stability. Specifically, CoP/NCF delivers a high reversible capacity of 335 mA h $g^{-1}$ at 0.1 A $g^{-1}$ and an excellent rate capability of 148 mA h $g^{-1}$ at 5 A $g^{-1}$, and CoSb/NCF exhibits a large capacity retention of 79.9% after 1000 cycles at 1 A $g^{-1}$. The strategy reported in this work may be able to be extended to other transition-metal compound/carbon composites, providing novel ideas and approaches for the synthesis of the anodes for PIB with high performance.

**Received 30 May 2021; accepted 6 July 2021; published online 31 August 2021**


1 Winter M, Barnett B, Xu K. Before Li ion batteries. Chem Rev, 2018, 118: 11433–11456
2 Wu K, Ling M, Zeng P, *et al.* Self-assembled multifunctional $Fe_3O_4$ hierarchical microspheres: high-efficiency lithium-ion battery materials and hydrogenation catalysts. Sci China Mater, 2021, 64: 1058–1070
3 Dunn B, Kamath H, Tarascon JM. Electrical energy storage for the grid: a battery of choices. Science, 2011, 334: 928–935
4 Yabuuchi N, Kubota K, Dahbi M, *et al.* Research development on sodium-ion batteries. Chem Rev, 2014, 114: 11636–11682
5 Li Y, Ji J, Yao J, *et al.* Sodium ion storage performance and mechanism in orthorhombic $V_2O_5$ single-crystalline nanowires. Sci China Mater, 2021, 64: 557–570
6 Zhang W, Sun Y, Deng H, *et al.* Dielectric polarization in inverse spinel-structured $Mg_2TiO_4$ coating to suppress oxygen evolution of Li-


  

rich cathode materials. Adv Mater, 2020, 32: 2000496
7 Rajagopalan R, Tang Y, Ji X, *et al.* Advancements and challenges in potassium ion batteries: a comprehensive review. Adv Funct Mater, 2020, 30: 1909486
8 Hosaka T, Kubota K, Hameed AS, *et al.* Research development on K-ion batteries. Chem Rev, 2020, 120: 6358–6466
9 Wang W, Ji B, Yao W, *et al.* A novel low-cost and environment-friendly cathode with large channels and high structure stability for potassium-ion storage. Sci China Mater, 2021, 64: 1047–1057
10 Xu Z, Du S, Yi Z, *et al.* Water chestnut-derived slope-dominated carbon as a high-performance anode for high-safety potassium-ion batteries. ACS Appl Energy Mater, 2020, 3: 11410–11417
11 Xu S, Yin Y, Niu H, *et al.* Adsorption and diffusion of alkali atoms on $FeX_2$ (X = Se, S) surfaces for potassium-ion battery applications. Appl Surf Sci, 2021, 536: 147774
12 Liao J, Hu Q, Mu J, *et al.* Introducing a conductive pillar: a polyaniline intercalated layered titanate for high-rate and ultra-stable sodium and potassium ion storage. Chem Commun, 2020, 56: 8392–8395
13 Ge X, Liu S, Qiao M, *et al.* Enabling superior electrochemical properties for highly efficient potassium storage by impregnating ultrafine Sb nanocrystals within nanochannel-containing carbon nanofibers. Angew Chem Int Ed, 2019, 58: 14578–14583
14 Chu Y, Guo L, Xi B, *et al.* Embedding MnO@$Mn_3O_4$ nanoparticles in an N-doped-carbon framework derived from Mn-organic clusters for efficient lithium storage. Adv Mater, 2018, 30: 1704244
15 Xiao Z, Huang YC, Dong CL, *et al. Operando* identification of the dynamic behavior of oxygen vacancy-rich $Co_3O_4$ for oxygen evolution reaction. J Am Chem Soc, 2020, 142: 12087–12095
16 Zhang Z, Du Y, Wang QC, *et al.* A yolk–shell-structured $FePO_4$ cathode for high-rate and long-cycling sodium-ion batteries. Angew Chem Int Ed, 2020, 59: 17504–17510
17 Zhou D, Yi J, Zhao X, *et al.* Confining ultrasmall CoP nanoparticles into nitrogen-doped porous carbon via synchronous pyrolysis and phosphorization for enhanced potassium-ion storage. Chem Eng J, 2021, 413: 127508
18 Lu X, Dong S, Chen Z, *et al.* Preparation of carbon coated $Ti_2Nb_2O_9$ nanosheets and its sodium ion storage properties. Acta Physico-Chim Sin, 2020, 36: 1906024
19 Wang S. Ultrathin carbon encapsulating transition metal-doped MoP electrocatalysts for hydrogen evolution reaction. Acta Physico-Chim Sin, 2020, 36: 2011013
20 Wang W, Jiang B, Qian C, *et al.* Pistachio-shuck-like $MoSe_2$/C core/shell nanostructures for high-performance potassium-ion storage. Adv Mater, 2018, 30: 1801812
21 Zhang T, Yang C, Sun S, *et al.* Mesoporous $Fe_3O_4$@C nanoarrays as high-performance anode for rechargeable Ni/Fe battery. Sci China Mater, 2021, 64: 1105–1113
22 Xu YH, Zhang BH, Gong GY, *et al.* Electrochemical properties study of $Sb_2O_3$ doped $Li_4Ti_5O_{12}$. Acta Physico-Chim Sin, 2006, 22: 1336–1341
23 Zhang W, Li B, Sun YG, *et al.* Spherical mesoporous metal oxides with tunable orientation enabled by growth kinetics control. J Am Chem Soc, 2020, 142: 17897–17902
24 Yi Y, Zhao W, Zeng Z, *et al.* ZIF-8@ZIF-67-derived nitrogen-doped porous carbon confined CoP polyhedron targeting superior potassium-ion storage. Small, 2020, 16: 1906566
25 Lai C, Zhang Z, Xu Y, *et al.* A general strategy for embedding ultrasmall $CoM_x$ nanocrystals (M = S, O, Se, and Te) in hierarchical porous carbon nanofibers for high-performance potassium storage. J Mater Chem A, 2021, 9: 1487–1494
26 Chen S, Feng Y, Wang J, *et al.* Free-standing N-doped hollow carbon fibers as high-performance anode for potassium ion batteries. Sci China Mater, 2021, 64: 547–556
27 Han J, Zhu K, Liu P, *et al.* N-doped CoSb@C nanofibers as a self-supporting anode for high-performance K-ion and Na-ion batteries. J Mater Chem A, 2019, 7: 25268–25273
28 Liu Q, Hu Z, Liang Y, *et al.* Facile synthesis of hierarchical hollow CoP@C composites with superior performance for sodium and potassium storage. Angew Chem Int Ed, 2020, 59: 5159–5164
29 Zhang C, Qiao Y, Xiong P, *et al.* Conjugated microporous polymers with tunable electronic structure for high-performance potassium-ion batteries. ACS Nano, 2019, 13: 745–754
30 Bai J, Xi B, Mao H, *et al.* One-step construction of N,P-codoped porous carbon sheets/CoP hybrids with enhanced lithium and potassium storage. Adv Mater, 2018, 30: 1802310
31 Sarkar S, Chaupatnaik A, Ramarao SD, *et al. Operando* sodiation mechanistic study of a new antimony-based intermetallic CoSb as a high-performance sodium-ion battery anode. J Phys Chem C, 2020, 124: 15757–15768
32 Liu Z, Li P, Suo G, *et al.* Zero-strain $K_{0.6}Mn_1F_{2.7}$ hollow nanocubes for ultrastable potassium ion storage. Energy Environ Sci, 2018, 11: 3033–3042
33 Jia B, Yu Q, Zhao Y, *et al.* Bamboo-like hollow tubes with $MoS_2$/N-doped-C interfaces boost potassium-ion storage. Adv Funct Mater, 2018, 28: 1803409
34 Wu H, Hou C, Shen G, *et al.* $MoS_2$/C/C nanofiber with double-layer carbon coating for high cycling stability and rate capability in lithium-ion batteries. Nano Res, 2018, 11: 5866–5878
35 Li P, Chen C, Ding S, *et al.* Controllable deposition of $FeV_2S_4$ in carbon fibers for sodium-ion storage with high capacity and long lifetime. Sci China Mater, 2021, 64: 1355–1366
36 Li Y, Qian J, Zhang M, *et al.* Co-construction of sulfur vacancies and heterojunctions in tungsten disulfide to induce fast electronic/ionic diffusion kinetics for sodium-ion batteries. Adv Mater, 2020, 32: 2005802

**Acknowledgements** This work was financially supported by the National Natural Science Foundation of China (22075147) and the Natural Science Foundation of Jiangsu Province (BK20180086).

**Author contributions** Zhou X conceived the overall concept and guided the whole writing. Xu J and Lai C carried out the synthesis, characterized the materials, analyzed the data, and wrote the paper. All authors contributed to the general discussion.

**Conflict of interest** The authors declare no conflict of interest.

**Supplementary information** Supporting data are available in the online version of this paper.

**Jingyi Xu** is currently an undergraduate student under the supervision of Prof. Xiaosi Zhou at the School of Chemistry and Materials Science, Nanjing Normal University. She was recommended to Tsinghua University and will start her PhD in September 2021. Her research interests include the fabrication of high-performance electrode materials for alkali-metal ion batteries.

**Xiaosi Zhou** received his BSc from Anhui University (2005) and PhD from the Institute of Chemistry, Chinese Academy of Sciences (ICCAS) (2010). He then conducted postdoctoral research in Prof. Robin D. Rogers' group at the University of Alabama, Prof. Yu-Guo Guo's group at ICCAS, and Prof. Xiong Wen (David) Lou's group at Nanyang Technological University. He is currently a Professor at Nanjing Normal University. His research interests focus on the design and synthesis of advanced electrode materials for alkali-metal ion batteries.

  

# 锚定于富氮掺杂碳纳米纤维中的超细CoP和CoSb纳米颗粒用于高效钾离子存储

徐静宜[†], 赖晨玲[†], 段丽平, 张郁萱, 徐一帆, 包建春, 周小四[*]

**摘要** 作为钾离子电池负极, 过渡金属化合物由于其高可逆容量和合适的电压平台而受到研究人员的广泛关注. 然而, 这些材料通常具有较差的导电性和超过80%的体积膨胀. 这些缺点往往会对电池的倍率性能和循环稳定性产生不利影响. 在本文中, 我们通过静电纺丝、碳化和磷化(锑化)成功地将超细CoP和CoSb纳米颗粒封装到富氮掺杂的碳纳米纤维中. 氮掺杂的碳纳米纤维有效防止了纳米颗粒聚集, 缓冲了充放电过程中CoP和CoSb的体积膨胀, 并提高了材料的导电性. 因此, CoP/氮掺杂的碳纳米纤维(CoP/NCF)负极表现出优异的钾离子存储性能, 包括335 mA h $g^{-1}$的可逆容量、长循环性能(在1 A $g^{-1}$下经1000次循环仍能保持79.3%的初始可逆容量), 以及在 5 A $g^{-1}$下148 mA h $g^{-1}$的优异倍率性能, 超过了大多数已报道的过渡金属化合物基钾离子电池负极材料.

  